

Understanding Component-Specific Contributions and Internal Dynamics in Silicon/Graphite Blended Electrodes for High-Energy Lithium-Ion Batteries

Christian Heubner,^{*[a]} Tobias Liebmann,^[b] Oliver Lohrberg,^[b] Sahin Cangaz,^[c] Sebastian Maletti,^[b] and Alexander Michaelis^[a, b]

Blended electrode materials containing high-capacity silicon (Si) and robust graphite (Gr) materials are considered advanced alternatives to pure graphite electrodes used in Li-ion batteries. Understanding the component-specific lithiation and delithiation behavior and electrochemical interactions between the blended materials is of crucial importance for targeted optimization of composition and microstructural design, yet hardly addressed to date. Herein, a model-like Si/Gr blended electrode and special electrochemical cell are introduced to directly capture the component specific behaviors for the first time. This includes studies of the formation cycles, the reaction

distribution between Si and Gr, the component-specific contributions to the capacity at different charge and discharge rates, and the internal dynamics during pulse loads and subsequent relaxation. The deconvolution of the components' behavior during operation provides fundamental insights that contribute to a profound understanding and targeted optimization of Si/Gr blended electrodes. Furthermore, the application of the presented experimental approach can serve scientists to identify and study other advanced materials combinations as blended electrodes for rechargeable batteries.

1. Introduction

The scheduled transition to electrified vehicles has created a significant demand for batteries with higher energy density per mass and volume than that of current Li-ion batteries (LIBs). Various approaches to improve energy density have been pursued, such as the development of high-capacity anode^[1,2] and cathode^[3,4] materials, improvements in electrode design^[5,6] and composition^[7–9] and the optimization of cell architecture.^[10,11] It was found that the development of high-capacity electrode materials has by far the greatest potential for optimization.^[12] In particular, silicon (Si) has emerged as the most promising high-capacity alternative (3580 mAh g^{-1} by formation of $\text{Li}_{15}\text{Si}_4$) compared to graphite (Gr, 370 mAh g^{-1} by formation of LiC_6), which is typically used as anode material in commercial LIBs.^[13,14] Due to the large volume changes during operation, which lead to particle pulverization and loss of electrical contact^[15–18] as well as unstable solid electrolyte

interphase (SEI),^[19–24] LIBs with Si anodes typically have a short cycle life, preventing commercialization. To address these challenges, several approaches are being pursued. This includes morphological considerations (nanoengineering),^[25–29] limited voltage window cycling and electrochemical balancing (variation of n/p ratio),^[30] development of binders with improved chemical and mechanical properties,^[23,31,32] and electrolyte additives for enhanced SEI stability.^[21,22] Furthermore, blended electrodes containing both Si and Gr are being developed to balance the beneficial and detrimental properties of the individual materials. This approach, combined with electrolyte additives such as fluoroethylene carbonate (FEC), which stabilize the SEI, greatly improved electrode cycle performance compared to pure Si electrodes.^[24,33,34] Accordingly, blended Si/Gr electrodes have attracted great attention in research and industry and are continuously developed further.^[35–38] However, in contrast to blended cathodes for LIBs,^[7,39,40] fundamental electrochemical interactions between the components of Si/Gr mixed anodes have hardly been investigated so far. This is because the detailed investigation and quantification of intra-electrode processes is a demanding experimental challenge due to the typical particle sizes in the submicron range.

Recently, Berhaut et al.^[41] and Yao et al.^[42] used operando X-ray scattering and operando energy dispersive X-ray diffraction, respectively, to investigate the interplay between Si and Gr in blended anodes. The determination of Li_xC_6 stages allowed to separate the respective capacities of Si and Gr during cycling and suggested component specific lithiation and delithiation mechanisms. Following these experimental results, Lory et al.^[43] studied Si/Gr blended anodes using a multi-scale porous electrode model. The simulations essentially confirm the component-specific lithiation and delithiation behavior

[a] Dr. C. Heubner, Prof. A. Michaelis
Fraunhofer Institute for Ceramic Technologies and Systems IKTS
01277 Dresden, Germany
E-mail: christian.heubner@ikts.fraunhofer.de

[b] T. Liebmann, O. Lohrberg, Dr. S. Maletti, Prof. A. Michaelis
Institute of Materials Science, TU Dresden
01062 Dresden, Germany

[c] S. Cangaz
Chair of Inorganic Chemistry 1, TU Dresden
01069 Dresden, Germany

 Supporting information for this article is available on the WWW under
<https://doi.org/10.1002/batt.202100182>

 © 2021 The Authors. *Batteries & Supercaps* published by Wiley-VCH GmbH.
This is an open access article under the terms of the Creative Commons Attribution License, which permits use, distribution and reproduction in any medium, provided the original work is properly cited.

proposed by Berhaut et al.^[41] and Yao et al.^[42] Furthermore, it is shown that the relative lithiation/delithiation is influenced by the applied current and the competition between different transport processes. Richter et al.^[44] recently studied low temperature charging and aging mechanisms of Si/Gr blended anodes using operando neutron scattering. Their results suggest that high charging rates led to lithiation of the Gr before Si compound due to kinetic limitations. Interestingly, the measurements indicate that during the subsequent relaxation period, Li-ions are transferred from Gr to Si. Very recently, Moon et al.^[45] revealed degradation mechanisms associated with Li crosstalk between Si and Gr using an analytical approach comparing Gr-only and Si/Gr blended anodes. This allows to quantify the amount of Li in Si and Gr depending on the SOC by means of operando XRD.

While the insights gained in previous studies are highly relevant for understanding and optimizing blended Si/Gr anodes, a common disadvantage of the methods used so far is their 'indirect' character, which requires some kind of calibration, validation and accurate input parameters (e.g. SOC dependent kinetic constants for modeling) that are usually not available or error prone. Furthermore, processes with fast kinetics might not be captured due to relatively long integration times. In order to gain more fundamental insights into the component-specific electrochemical behavior and internal dynamics of blended electrodes, we developed an experimental setup including a model-like blended electrode, which allows a direct recording of the electrochemical interactions between the components.^[40,46,47] This setup is used herein for the first time to study the lithiation and delithiation behavior of Si/Gr blended electrodes using a model system of particulate graphite and columnar Si. The investigations include studies of the formation cycles, the reaction distribution between Si and Gr, the component-specific contributions to the capacity at different charge and discharge rates, and the internal dynamics during pulse loads and subsequent relaxation. While specific quantitative aspects will of course depend on the actual nature

and morphology of the components as well as the composite properties and blended-electrode design, the exemplary deconvolution of the components' behavior during operation shown here provides fundamental insights that can contribute to a deeper understanding and targeted optimization of composition and microstructure. Furthermore, with this work we would like to encourage scientists to adapt our straightforward approach and perform advanced studies on blended anodes to gain insights into component-specific contributions and to optimize the materials in a targeted manner. In this sense, the present work is not only an exemplary study on a specific model system, but can also serve as inspiration for studies on other blended anodes, such as CuO/CNT,^[48,49] Sn/C,^[50,51] and SnS₂/rGO.^[52,53]

2. Results and Discussion

Figure 1 illustrates the approach of studying the individual behaviors of Si and Gr in blended anodes. The experimental setup used to unfold the component-specific electrochemical behavior was described and validated comprehensively in the context of blended cathodes for LIB.^[40,46,47,54] In brief: in a blended electrode, the different active materials are short-circuited by physical contact, conductive additives, or the current collector foil. From a thermodynamic point of view, this situation is identical to the case where several electrodes are short-circuited with a low-resistance connection. Based on these considerations and inspired by experimental methods in bimetallic corrosion research, we use several separate but short-circuited single-component electrodes to form a model-like blended electrode (MLBE). Figure 1 includes schematics of the cell design and the electrical network for recording the individual electrochemical behaviors of the components in the MLBE. The working electrode holder is made of PCTFE (CF_2CClF_2) and is provided with holes to accommodate four electrically insulated current collectors. Assembling of the cell is

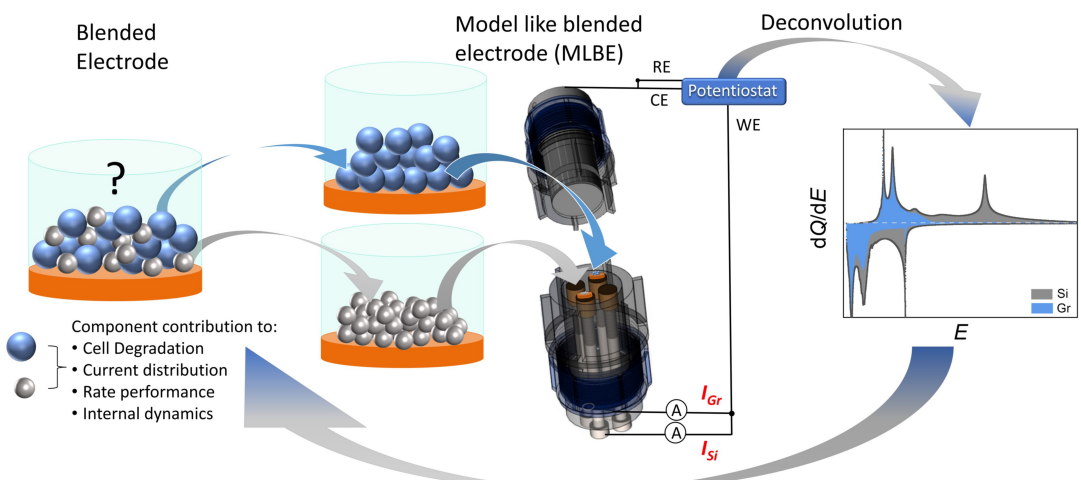


Figure 1. Schematic representation of the approach of this study: Single component electrodes are connected in parallel as the working electrode in an electrochemical cell. External shorting via low-impedance ammeters forms a model-like blended electrode (MLBE) that allows deconvolution of the component specific lithiation and delithiation currents during operation and observation of any internal dynamics among the components of the blend.

done by placing single component Si and Gr electrodes in the working electrode holder, which are then shorted externally via low-impedance ammeters to form the MLBE. This allows deconvolution of the component specific lithiation and delithiation currents during operation and observation of any internal dynamics among the components of the blend. The Si and Gr electrodes used to form the MLBE were investigated in detail previously.^[55–58] Additional information on electrode preparation, cell assembly and material characterization are provided within the experimental section and as Supporting Information.

2.1. Formation Cycles

Figure 2a shows the electrode potential of an MLBE ($m_{\text{Si}}:m_{\text{Gr}}$ 1:13) during the first lithiation cycles. The first and the second cycle slightly differ regarding the slope and plateau positions of the electrode potential. These differences are mainly caused by SEI formation and irreversible structural changes of Si.^[59] The second and third cycle hardly differ, indicating completion of SEI formation and stable cycling behavior of the MLBE. Figure 2b and c compare the deconvoluted differential capacity of the first and the second cycle, showing the individual

contributions of Si and Gr to the electrode reaction. The first lithiation shows a sharp reduction peak at 200 mV that originates from Li insertion into amorphous Si (a-Si). Subsequently, two further Si reduction peaks at 70 mV and 30 mV indicate the formation of a-Li_xSi and a two-phase reaction between a-Li_xSi and crystalline Li₁₅Si₄.^[60] Additionally, Gr starts to contribute to the electrode reaction, showing pronounced reduction peaks at 67 mV and 27 mV. Lithiation in the potential range 150–10 mV is characterized by simultaneous Li incorporation in Si and Gr. In contrast, distinct peaks are found in this potential range for the oxidation reaction, which are exclusively attributed to the delithiation of Gr. Si starts to contribute to the oxidation reaction at about 230 mV via re-formation of a-Si from a-Li_xSi. After a narrow potential range in which Si and Gr react simultaneously, Si dominates the oxidation reaction for potentials above 300 mV, where a compressed oxidation peak appears, indicating the transition from amorphous Li_{3.16}Si to Li_{2.33}Si.^[61] A pronounced oxidation peak related to the dealloying of crystalline Li₁₅Si₄ is observed at 450 mV,^[62] accounting for the smooth plateau at 450 mV during charge in the voltage profile (Figure 2a). This behavior is expected since the lower cutoff voltage is set below 50 mV (cf. Figure S3),^[63] leading to formation of crystalline Li₁₅Si₄ in thick Si film electrodes.^[64] The oxidation behavior is similar in the subsequent cycles, whereas

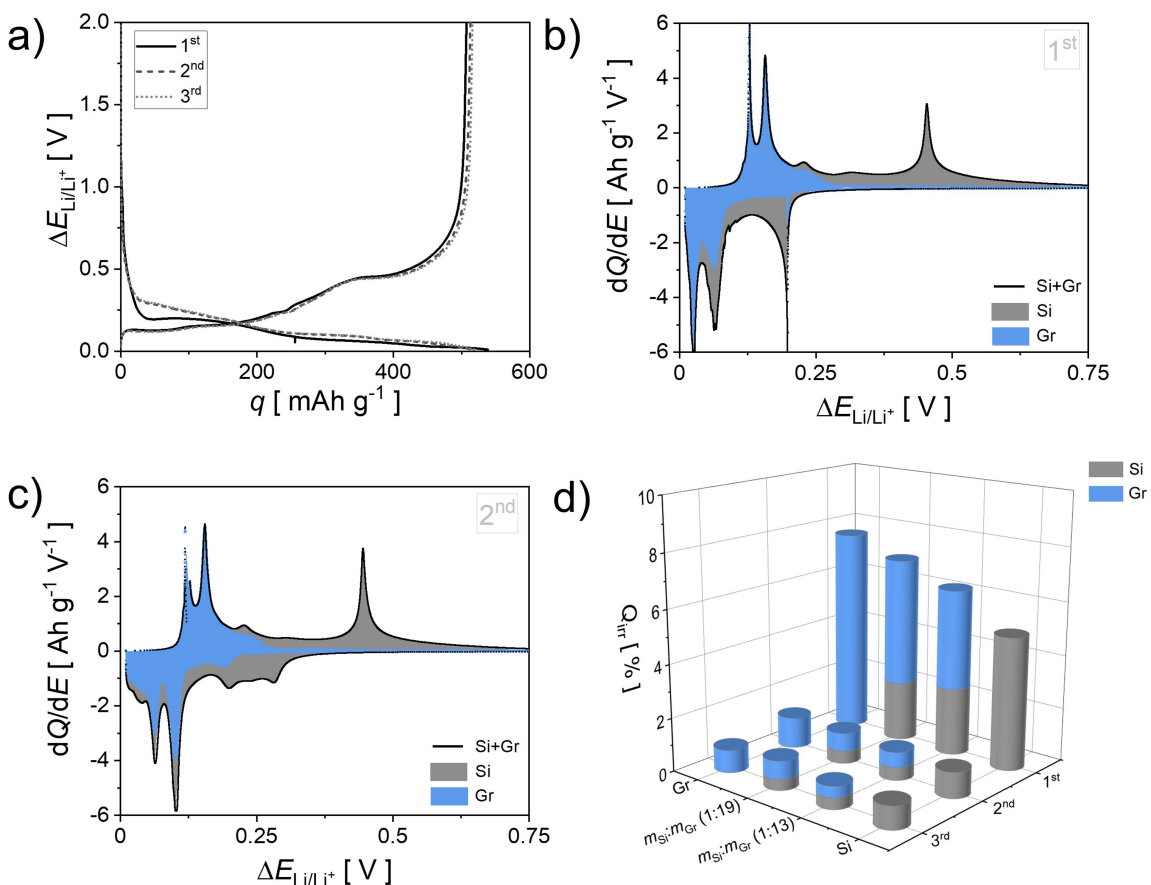


Figure 2. a) Potential profiles during initial cycling of a model-like Si/Gr electrode ($m_{\text{Si}}:m_{\text{Gr}}$ 1:13). Deconvoluted differential capacity of the b) first and c) second cycle, showing the individual contributions of Si and Gr to the electrode reaction. d) Component specific coulombic inefficiency (relative capacity loss) of the first cycles depending on the mass ratio Si:Gr.

the reduction behavior differs (Figure 2c). Besides some slight shifts of the reduction peaks of Gr, main differences are found in the behavior of Si. In the second lithiation, at least two strongly overlapping reduction peaks are found in a potential range of 300–200 mV, replacing the sharp peak observed during the first cycle. The sharp reduction peak located at 230 mV can be attributed to resistive behavior of virgin amorphous silicon, which highly impedes Li⁺ penetration over first lithiation.^[29] Thereafter, it turns into two flattened reduction peaks in the following lithiation, referring to formation of a-Li_xSi binary phases and hence indicating amorphization and electrochemical activation of Si. Note that, at around 230 mV, other events take place such as SEI formation,^[65] reduction of SiO surface film^[66] and formation of lithium silicates,^[67] contributing also to the sharp reduction peak.

Figure 2d shows the contributions of the components to the Coulombic inefficiency (relative capacity loss) of the first cycles depending on the mass ratio Si:Gr. In the present example, the pure graphite electrode shows the largest capacity loss (7.6%) in the first cycle, whereas Si only exhibits a Coulombic inefficiency of 4.9 %. As expected, the Coulombic inefficiency of the blended electrodes ranges between that of the components with respective contributions of Si and Gr depending on the mass ratio and corresponding share in capacity. The capacity loss during the first cycle is mainly due to the reductive decomposition of the electrolyte at low potentials and the consequent SEI formation.^[68] Dahn et al.^[69] showed that capacity loss due to SEI formation is proportional to the electrochemically active surface area of the electrode. In the present case, the specific surface areas of the particulate Gr and the columnar Si with respect to the specific capacity are roughly estimated from SEM images to $S_{\text{Gr}} = 20 \text{ cm}^2 \text{ mAh}^{-1}$ and $S_{\text{Si}} = 1 \text{ cm}^2 \text{ mAh}^{-1}$ (cf. Figures S1 and S4). Thus, the lower Coulombic inefficiency of pure Si compared to Gr is mainly attributed to the smaller surface area that is passivated by SEI formation with respect to the specific capacity. In the blended electrodes, Si makes a significant contribution to the capacity, even though the mass fraction is relatively small. According to this contribution, a corresponding fraction of the Coulombic inefficiency is established in the blended electrodes, which is consistent with theoretical estimations based on the components' properties (cf. Figure S8). In subsequent cycles, the Coulombic inefficiency drops to about 0.9% for both Gr and Si, indicating that the SEI formation is mostly complete. Also in this case, the behavior of the blended electrodes meets expectations based on the weighted superposition of the components' properties.

As discussed above, the amount of electric charge consumed during SEI formation and the Coulombic efficiency for continuous cycling depends on the electrochemically active electrode area and specific surface chemistry. Therefore, the quantitative aspects shown in Figure 2d are not representative for any possible Si/Gr blend but for the present example of micron sized graphite particles and columnar Si. Depending on the specific area and surface chemistry, the contributions of Si and Gr to SEI-losses and Coulombic efficiency of the blended electrode might differ substantially. With the experimental

approach presented here, these relationships can be studied and understood in a straightforward manner. Note that a comparable setup can be realized by connecting several half cells in parallel, e.g. in Swagelok cells or coin cells. Indeed, we have found that this gives similar results compared to the custom-built MLBE cell shown in Figure 1. The main difference between these configurations is the isolated electrolyte compartments, which could compromise the long-term cycling due to cross-contamination or uneven cell drying. Nevertheless, the study of half-cells with single-component electrodes connected in parallel is considered an extremely simple approach and is recommended in the absence of special measurement setups to deepen the understanding of blended electrodes.

2.2. SOC-dependent Reaction Distribution

After initial cycling, the potential profile, achieved capacity and Coulombic efficiency become constant (cf. Figure 2). Figure 3 shows the electrode potential of an MLBE ($m_{\text{Si}}:m_{\text{Gr}} = 1:13$), the specific currents related to competing electrochemical reactions of Si and Gr and the corresponding accumulated capacities in the course of lithiation and delithiation. Initially, the lithiation current is higher at Gr but decreases to almost zero during the first stages of lithiation. Accordingly, Si dominates the electrode reaction at low SOC. At SOC = 0.25, the contribution of Gr to the electrode reaction increases again. The further course of lithiation is characterized by alternations between the competing Li insertion in Gr and Si. This behavior results from the superposition of the differential capacities (dQ/dV) of Si and Gr (Figure 2c) that vary with the SOC and potential, respectively. Particularly, first-order phase transitions in the course of lithiation or delithiation are accompanied by a constant potential and high differential capacity (dQ/dV).^[70,71] Accordingly, a component passing through a two-phase region dominates the electrode reaction in the corresponding SOC or potential region. During lithiation at potentials > 220 mV, the intercalation capacity of Gr is much lower than that of Si. Accordingly, lithiation of the MLBE is dominated by Li alloying of Si. By passing the 220 mV potential plateau of Gr, marking the $\text{LiC}_{72} \rightarrow \text{LiC}_{36}$ biphasic region,^[72,73] the contribution of Gr to the electrode reaction starts to increase. After completion of the phase transition and the associated reduction of the differential capacity of Gr, the proportion of Si in the electrode reaction increases again. Subsequently, lithiation of Gr dominates again when passing through the biphasic regions $\text{LiC}_{24} \rightarrow \text{LiC}_{12}$ (110 mV plateau) and $\text{LiC}_{12} \rightarrow \text{LiC}_6$ (85 mV plateau).^[72,73]

In the case of delithiation, the current distribution between Si and Gr is not simply mirror inverted to the behavior during lithiation. Rather, there is a sharp separation between two SOC regions clearly dominated by Gr (0.65 < SOC < 1.0) and Si (0.05 < SOC < 0.5). Considering the deconvoluted differential capacity dQ/dV (Figure 2c), the differences between lithiation and delithiation are caused by the much larger potential hysteresis of Si when compared to Gr. In the case of Gr, the difference between the characteristic redox potentials during

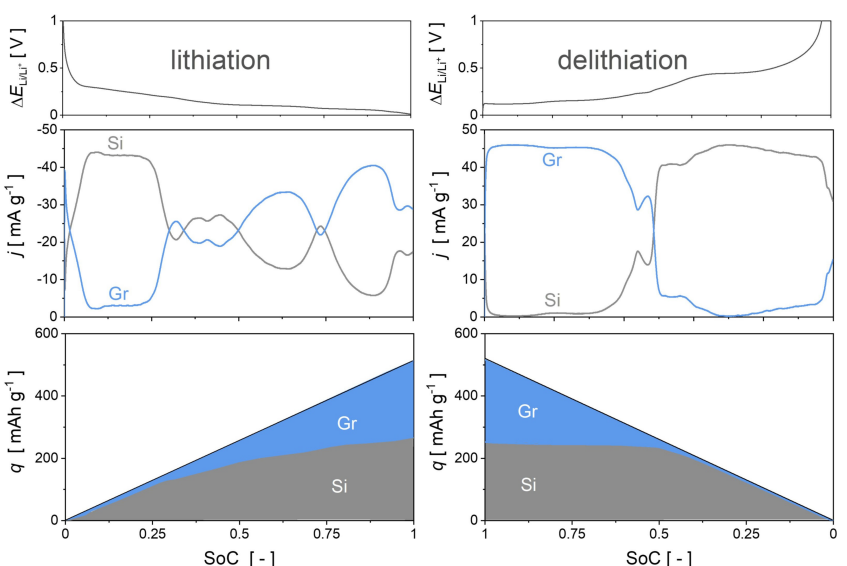


Figure 3. Potential profiles (top), specific currents (middle) and specific capacity contributions (bottom) related to the competing electrochemical reactions of Si and Gr in a MLBE ($m_{\text{Si}}:m_{\text{Gr}}$ 1:13) during lithiation (left) and delithiation (right).

lithiation and delithiation is less than 50 mV (cf. Figure 2c). Si shows lithiation activity below 300 mV. Delithiation starts at 230 mV but becomes significant only at potentials ≥ 450 mV. The large potential hysteresis of Si is usually attributed to stress-potential coupling, i.e. additional mechanical work required for delithiation of the stressed material that underwent large volume expansion.^[59] As a result, the differential capacities of Si and Gr hardly overlap during delithiation, which causes the differences in the competing lithiation and delithiation behavior (Figure 3a and b). This behavior agrees with recent literature reports based on indirect methods^[41,42] and confirms theoretical predictions based on a multi-scale porous electrode model.^[43] We want to emphasize that the present approach to separate the contributions of Si and Gr includes some specific advantages over previous experimental reports: i) precise and direct quantification of the individual lithiation and delithiation currents, ii) high sampling rate (1 Hz), allowing to capture processes with fast kinetics and iii) quantitative insights into internal dynamics, such as Li-redistribution between Si and Gr. In the following we make use of these advantages and investigate the contributions of Si and Gr to the capacity of the MLBE depending on the charge/discharge rate for varying mass ratios. Furthermore, internal dynamics during pulse loads and subsequent relaxation are analyzed.

2.3. Rate Performance

To understand individual contributions of Si and Gr to the rate capability of Si/Gr blended electrodes, rate performance tests based on chronoamperometry^[74,75] were carried out using Si/Gr MLBE. Figure 4a shows the deconvoluted capacity as a function of the C-rate obtained from a Si/Gr MLBE ($m_{\text{Si}}:m_{\text{Gr}}$ 1:19) for the case of lithiation. At low currents (<0.2C), Si and Gr contribute

to the capacity of the blended electrode according to theoretical expectations based on the mass proportions in the mixture. As the current increases, the contribution of Gr drops more than that of Si, suggesting that Si has the better rate capability. In this context, we would like to emphasize that the rate capability of battery electrodes is determined not only by the material itself but also by the particle size and shape, electrode design, electronic and ionic wiring, contact resistances, etc.^[76] Accordingly, the differences present between the rate capability of Si and Gr need not necessarily be due to intrinsic material properties. For currents above 1C, the available capacity approaches zero in the case of lithiation. In contrast, delithiation yields almost full capacity for rates below 10C. This suggests different rate limitations for lithiation and delithiation.

Lithiation is accompanied with electrolyte depletion in the porous electrode. The Li concentration in the electrolyte drops from the initial 1M to zero when approaching the so-called diffusion limited C-rate.^[77] For delithiation, such a limit does not exist. High lithium concentration in the electrolyte might slow down the charge transfer reaction or even culminating in salt precipitation. However, this is expected to require much larger changes in concentration to yield a significant effect when compared to lithiation, thus, allowing higher C-rates. Furthermore, the range of overvoltage, and thus the driving force of the reaction, is different for lithiation and delithiation. The average potentials of the blended anodes amount to 216 mV vs Li/Li⁺ ($m_{\text{Si}}:m_{\text{Gr}}$ 1:19) and 240 mV vs Li/Li⁺ ($m_{\text{Si}}:m_{\text{Gr}}$ 1:13). The lithiation cutoff potential was set to 10 mV to avoid Li plating and the delithiation cutoff potential was 2 V. Accordingly, the range of acceptable overvoltage for delithiation is much larger, resulting in larger currents, when compared to lithiation.

Apart from that, Si seems to have slightly higher rate capability in the case of delithiation as well. The capacity of Gr

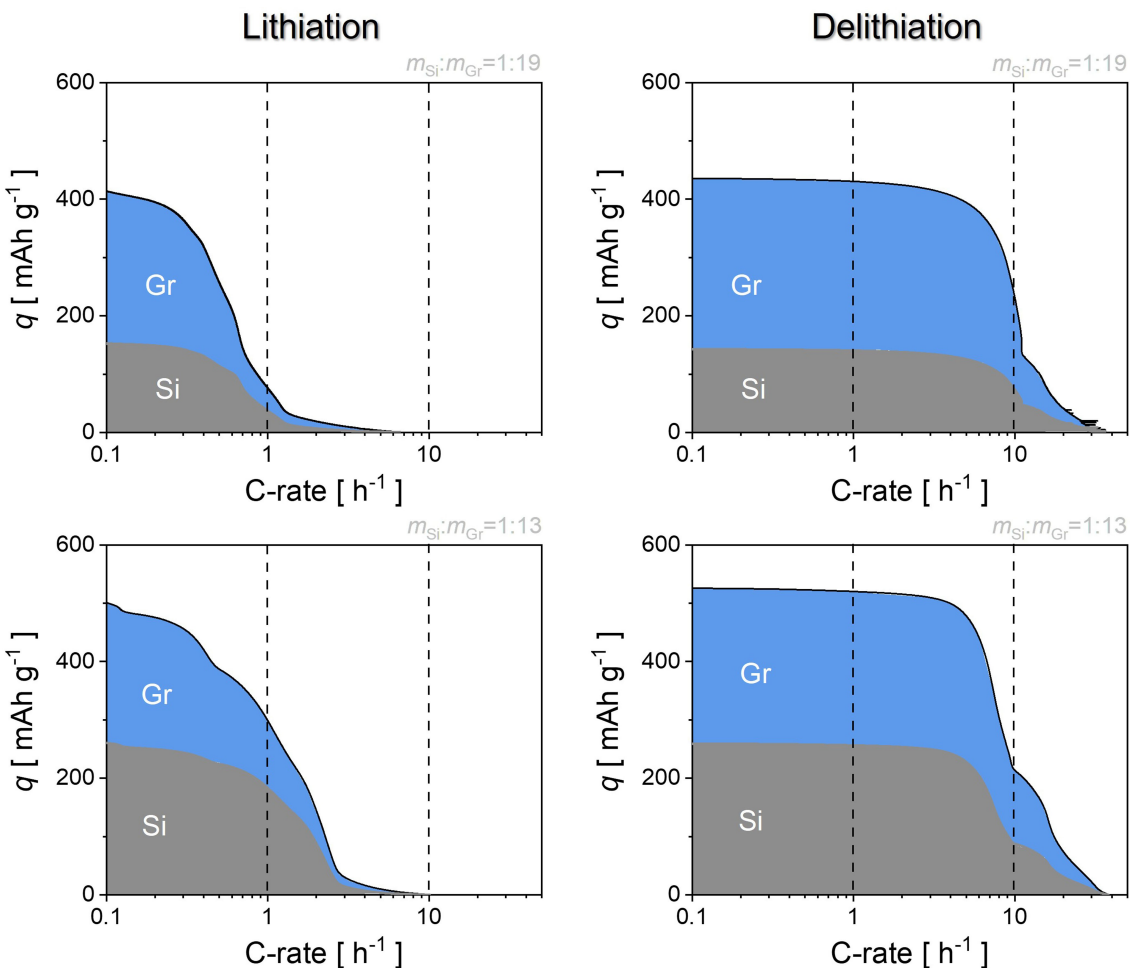


Figure 4. Deconvoluted rate performance for lithiation (left) and delithiation (right) of Si/Gr MLBE of different mass ratios, $m_{\text{Si}}:m_{\text{Gr}} = 1:19$ (top) and $m_{\text{Si}}:m_{\text{Gr}} = 1:13$ (bottom).

collapses somewhat faster, which means that the proportion of Si to the electrode capacity increases at high C-rates. Interestingly, increasing the mass ratio of Si noticeably increases the rate capability of the blend in the case of lithiation (Figure 4c) but hardly affects the behavior for delithiation (Figure 4d). The improvement of the lithiation rate capability can be assigned to the better kinetics of the Si when compared to Gr. The larger the proportion of Si, the higher the rate capability of the blend. Considering this, the fact that larger Si proportions do not influence the delithiation rate capability suggests that the rate limiting mechanism in this case is not depending on the actual material used but on concomitant effects. Interestingly, in the case of the MLBE used, the difference in rate capability between the different compositions is much smaller when the achieved capacity is plotted versus current density instead of C-rate (Figure S9). This most likely results from the compensation of negative and positive effects associated with changes in specific capacity and surface area as a function of composition. As noted above in the context of SEI formation and Coulombic efficiency, the quantitative aspects shown in Figure 4 are not representative for any possible Si/Gr blend but for the present example of micron sized graphite particles and columnar Si.

The contributions of Si and Graphite, their individual rate capability and the resulting performance of the blended electrode depend on several aspects and thus might vary substantially for different blended electrodes. Nevertheless, the present results show that the deconvolution of the components' contributions supports the understanding of rate limitations in blended Si/Gr anodes. We would also like to point out that the developed model setup aims to provide basic information about the behavior of Si and graphite during charging and discharging. In real Si–Gr mixtures, more complex interactions may exist compared to the model setup, which may lead to a different behavior, e.g. in terms of rate capability. One of the most critical problems in mixing Si and Gr is the loss of electrical conductivity of the composite due to the different volume change of Si~300% and Gr~10%.^[78] Thus, materials which are very stable as single electrodes can show poorer performance in the mixture. In this case, it is typically helpful to use some long-range conductive additives such as carbon nanotubes or nanofibers.^[79,80]

2.4. Internal Dynamics

Studies on blended Li-insertion cathodes suggest a so-called ‘buffer effect’ where a component with fast reaction kinetics acts as an internal pathway, carrying the current for a more rate-limited constituent at high loads.^[54] Recently, based on operando neutron scattering measurements, Richter et al. proposed a similar internal redox mechanism in blended Si/Gr anodes.^[44] For the quantitative proof of the propagated effect, experiments with different pulse loads were performed using a Si/Gr MLBE ($m_{\text{Si}}:m_{\text{Gr}}$ 1:13). Figure 5 shows potential transients during lithiation pulses (12% of cell capacity) and subsequent relaxation as well as the specific currents related to the individual constituents. At low C-rates (0.2C), the electrode potential decreases to approximately 0.22 V at the end of the lithiation pulse (Figure 5a). Initially, the current is consumed by Gr to a large extent. With ongoing lithiation, the contribution of Si increases and levels off at approximately 84 mA g^{-1} , which corresponds to 91% of the applied current. This behavior is consistent with expectations based on thermodynamic considerations regarding the superimposed differential capacities of Gr and Si. At very low SOC or high potentials, the differential capacity of Gr is larger than that of Si. Accordingly, Gr initially dominates lithiation and the electrode potential decreases until the redox potential of Si is reached. Then, the differential capacity of Si is much higher than that of Gr. Accordingly, the proportion of the current consumed by Si makes up the main contributor. During the relaxation period, the electrode potential tends towards approximately 0.3 V. While, the net current is zero in the relaxation period, the MLBE allows

capturing the internal dynamics between Si and Gr. After interruption of the external load, a negative current is observed at Si, indicating a reduction reaction. At the same time, an oxidative current occurs at Gr, which exactly cancels the current drawn from the Si. This indicates that a small amount of Li is extracted from the Gr and inserted into Si during the relaxation period. The integration of the current indicates that the specific charge redistributed between Si and Gr amounts to approximately 5 mAh g^{-1} , which corresponds to 8% of the specific charge applied during the 0.2C lithiation pulse.

At the 2.0C rate, the electrode potential decreases to 0.05 V at the end of the lithiation pulse (Figure 5b). Again, Gr dominates lithiation at the beginning and the contribution of Si increases with ongoing lithiation. However, in this case, the contribution of Si levels off at approximately -580 mA g^{-1} , which corresponds to 63% of the applied current. Thus, the contribution of Gr is much larger when compared to the 0.2C rate. After interruption of the current, a two-step relaxation transient is observed. First, the electrode potential forms a plateau at approximately 0.26 V followed by a second potential transient approaching approximately 0.33 V at the end of the relaxation period. Actually, the electrode potentials at the end of the relaxation period after the 0.2C and 2.0C pulses should be identical. The difference of about 0.03 V is most likely due to the relatively low differential capacity in this potential range. This leads to the fact that smallest differences in the initial SOC or the SOC change during the pulse cause significant potential differences, which, however, has no significant influence on the findings regarding the internal dynamics of the Si/Gr blends. In contrast to the behavior at low rates, much larger reduction

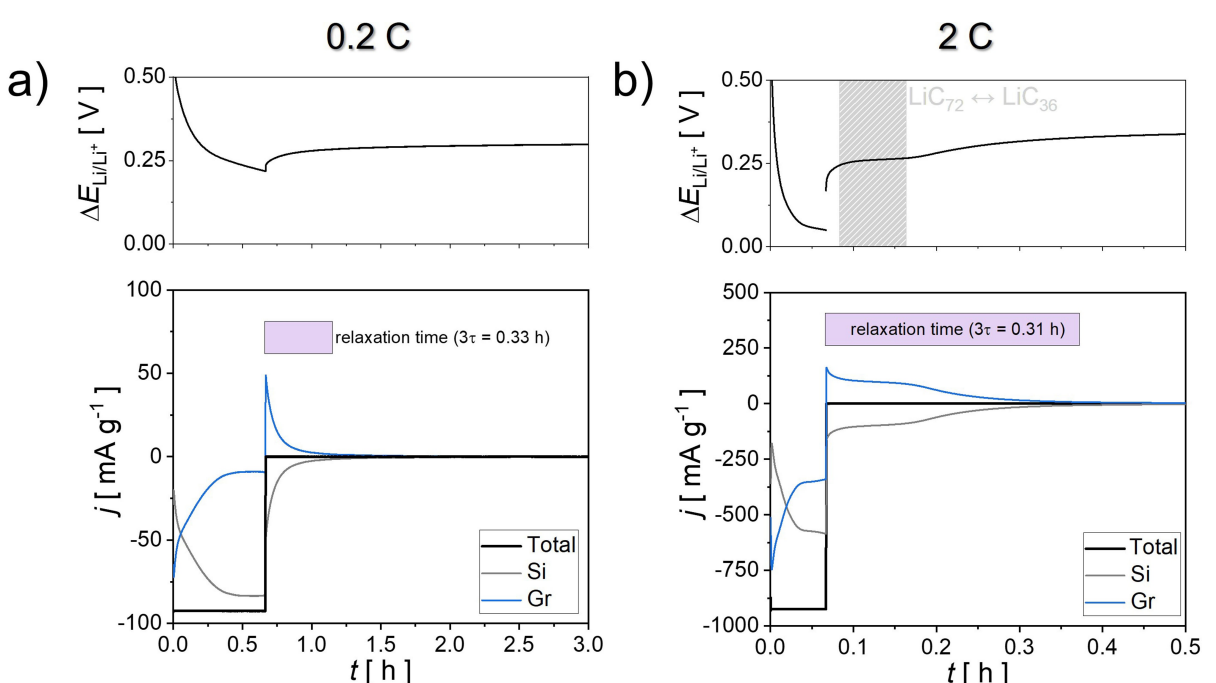


Figure 5. Internal dynamics between Gr and Si in a MLBE ($m_{\text{Si}}:m_{\text{Gr}}$ 1:13) during pulse loads and subsequent relaxation. Electrode potential (top) during lithiation and subsequent relaxation, and deconvoluted currents (bottom) related to lithiation (reduction) or delithiation (oxidation) of Gr and Si, at a) 0.2C for 2400 s ($\Delta q = 61 \text{ mA h g}^{-1}$) and b) 2.0C for 240 s ($\Delta q = 61 \text{ mA h g}^{-1}$). The purple bars represent the relaxation time until the current is reduced to 5% of the maximum current.

and oxidation currents are observed at Si and Gr after the 2.0C pulse. Furthermore, the current transients exhibit a plateau region that coincides with the potential plateau during the relaxation period. The integration of the current indicates that the specific charge redistributed between Si and Gr amounts to approximately 18.4 mAh g^{-1} , which corresponds to 30% of the specific charge applied during the lithiation pulse. Analysis of the relaxation times shows that they do not vary significantly for the different pulse loads. This suggests that there are no serious differences in the relaxation mechanism despite the extent of redistributed Li.

Figure 6 depicts a schematic illustration of pulse and relaxation mechanisms occurring in Si/Gr blended electrodes at high and low lithiation rates. At low C-rate, the electrode potential is close to the equilibrium potential and lithiation takes place according to thermodynamic expectations based on the superposition of the differential capacities of Si and Gr. The electrode reaction is mainly dominated by Si, since the differential capacity of Gr is small for electrode potentials $> 220 \text{ mV}$, when compared to Si. During relaxation, concentration gradients in the solid (Si) and the electrolyte are balanced and the open-circuit potential tends towards a new steady state value. Small amounts of Li originally intercalated in Gr are re-extracted and transferred to Si until the equilibrium potentials of the constituents are identical.

At high C-rates, the distribution of lithiation current between Gr and Si is no longer determined by thermodynamic aspects alone, but also by kinetic factors. In this case, the electrode potential is significantly lower than the equilibrium potential due to the overvoltage caused by ohmic, charge transfer, and diffusion limitations. Consequently, the electrode potential exceeds the Gr intercalation potential (220 mV) and the contribution of Gr to the electrode reaction increases

significantly. During the relaxation period, concentration gradients in the solid particles (Si and Gr) and the electrolyte are balanced. This process, together with the disappearance of the overvoltage, causes the potentials of Si and Gr to drift apart according to their Li content-dependent equilibrium potentials. The emerging difference in Gibbs energy drives the redistribution of Li-ion among the components. Li is extracted from Gr (oxidation reaction) and inserted into Si (reduction reaction). During this process, the electrode potential is a mixed potential of Li extraction from Gr and Li incorporation into Si (cf. Figure 5b). Graphite passes through a two-phase region ($\text{LiC}_{72} \leftrightarrow \text{LiC}_{36}$) in this potential range, which is characterized by a plateau at 220 mV. Accordingly, during the Li rearrangement in the relaxation phase, the mixed potential is constant until the phase transformation of graphite is completed. Subsequently, the equilibrium potentials of Si and Gr converge. The Li^+ rearrangement current approaches zero and the electrode potential reaches a new equilibrium value. This equilibrium state is identical to the behavior at low C-rates, although the reaction path is different. This behavior basically agrees with the findings of Richter et al. based on operando neutron scattering measurements.^[44] The analyses performed here extend existing knowledge by providing direct quantification and measurement of fast internal dynamics, allowing deeper insights into the buffering of high pulse loads. The fundamental understanding of these internal rearrangement processes can support the targeted design of blended Si/Gr anodes to enhance the fast-charging capability of future batteries. In addition, targeted exploitation of this ‘buffer effect’ could help to avoid unwanted Li plating at high charging rates or low temperatures. The approach of a model-like blended electrode presented here appears to be well suited to support such developments.

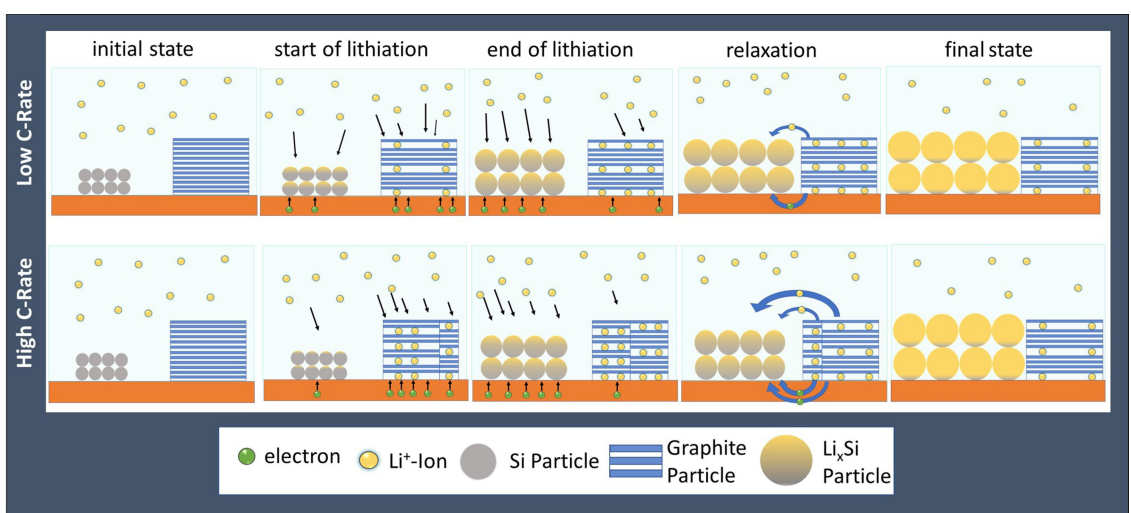


Figure 6. Graphical representation of pulse and relaxation mechanisms in Si/Gr blended electrodes for different lithiation conditions. Low lithiation rate: lithium is initially incorporated mainly in Gr and then exclusively in Si; during the relaxation phase, the Li^+ concentration gradients in the solid and electrolyte are balanced; small amounts of Li originally intercalated in Gr are re-extracted and transferred to Si until their equilibrium potentials are identical. High lithiation rate: After a transient phase, lithium is incorporated into both Si and Gr; the increased lithiation of Gr causes the formation of a second Li-rich phase LiC_{36} next to LiC_{72} ; during the relaxation phase, the amount of LiC_{36} is reduced by transferring Li to Si until finally the same final state is reached as at the low lithiation rate.

3. Conclusion

The component-specific electrochemical behavior and internal dynamics of blended Si/Gr electrodes are investigated using a model-like blended electrode consisting of particulate graphite and columnar Si. The deconvoluted capacity losses by SEI formation during the first cycles agree with expectations based on the behavior of the pure components. Studies of the SOC-dependent reaction distribution reveal a complex interplay between the dominance of Gr and Si during lithiation. Gr particularly dominates the electrode reaction at certain potentials when passing through two-phase regions. Si dominates where Gr shows solid solution behavior and at high potentials where the differential capacitance of Gr is low. In contrast, during delithiation, a clear separation of the redox activity of Si and Gr is evident. The asymmetry between charging and discharging is caused by the much larger potential hysteresis of Si compared to Gr. These observations support the behavior proposed based on operando measurements and simulations. The method used here is the first to provide unequivocal evidence of this behavior, since lithiation and delithiation currents and the resulting lithiation states of Si and Gr are determined directly without the need for calibration or any kind of input parameters. Moreover, the MLBE approach allows to detect smallest features and changes of the competing electrochemical reactions of Si and Gr in blended anodes, which can be highly useful, e.g. to study component specific degradation.

The deconvolution of the component specific contributions to the capacity at different rates shows that, in the present example, Si provides higher rate capability. Thus, the higher the Si content in the blend, the higher the rate performance. Studies of internal dynamics show significant electrochemical interactions between Gr and Si, depending on the applied current. Notably, at high currents, a component with fast reaction kinetics or suitable potential plateau can act as an internal pathway carrying the current for a more rate-limited component. During the subsequent relaxation phase, lithium is redistributed between the components. This behavior results from thermodynamic factors of the emerging and converging equilibrium potentials of Si and Gr during charge/discharge and subsequent relaxation, respectively, and enables the fabrication of anodes with high energy density but also very good rate capability. The extent of the observed buffer effect depends on a variety of parameters, such as the effective kinetics of the components, the inter-particle contact/distance and morphological aspects. Similarly, the individual rate performance depends not only on intrinsic material properties, but also on electrode design, composition (e.g. content of conductive additives) and electrolyte properties. Accordingly, the quantitative aspects of the results shown here do not apply to all possible Si/Gr anodes but illustrate the importance of these effects, which should be considered when developing composition and design of advanced blended electrodes. Comparable investigations can also be performed without the custom-made cell applied here by connecting several half cells with single-component electrodes in parallel. Therefore, we

would like to encourage scientists to adapt this straightforward approach and perform advanced studies on specific blended anodes to gain insights into component-specific contributions and to optimize the materials in a targeted manner. In this sense, the present work is not only an exemplary study on a specific model system but can also serve as inspiration for studies on other advanced material combinations as blended anodes for rechargeable batteries.

Experimental Section

Materials and electrode preparation

The graphite electrodes investigated in this study were received from a commercial supplier (MTI Corp.). The 50 µm thick electrodes were made of the 94.5% active material graphite and 5.5% binder (styrene-butadiene rubber and carboxymethyl cellulose) coated onto a copper current collector.

Amorphous silicon electrodes were fabricated via deposition in a batch process by DC magnetron sputtering at argon pressure of 0.3 Pa (MSL600, Fraunhofer IWS). As sputtering target a 5 N polycrystalline silicon target has been used to deposit 5–7 micron thick silicon layers (Figure S1) onto 10 µm thick dendritic copper foils (SE-Cu 58, Schlenk Metallfolien GmbH & Co. KG) in a temperature controlled process at room temperature. The Si loading was ca. 0.90 mg cm⁻², corresponding to an areal capacity of ~3.2 mAh cm⁻².

Cell assembly and electrochemical measurements

The electrochemical cells were assembled in an argon filled glovebox (<1 ppm H₂O, <2 ppm O₂). A Li-foil (99.9% trace metal basis, ALDRICH Chemistry) served as counter electrode. A shorted Si electrode and Gr electrode acted as the working electrode. The separator was a borosilicate glass-microfiber filter (CAT No. 5401–090 E, Whatman). High purity 1 M LiPF₆ dissolved in a 1:1 wt% ratio mixture of ethylene carbonate and dimethyl carbonate (LP30 Selectlyte, Merck) with additional 20 wt% fluoroethylene carbonate (Alfa Aesar, 98%) was used as electrolyte. The electrochemical measurements were carried out using a potentiostat (VMP3, Biologic). The short-circuit currents between the working electrodes were measured via high accuracy ammeters (2100 6.5-Digit USB Digital Multimeter, KEITHLEY). First, the model-like blended electrodes were cycled three times with a constant current of 0.1C between 0.01 V and 2 V. After this initial cycling, chronoamperometric measurements were carried out from the fully delithiated state by applying the 0.01 V cutoff voltage and recording the current transient. After this step, another chronoamperometric step was carried out by applying 2 V cutoff voltage and recording the current. The internal dynamics were investigated by charge-controlled current pulse experiments. A 0.2C lithiation pulse was applied to the cells from the fully delithiated state at 12% of the total capacity with subsequent measurement of the current density distribution in the relaxation phase. This experiment was repeated with the same total charge for a 2C lithiation pulse. The C-rates are based on the theoretical capacity of the Si/Gr mixtures. These were determined via weighted averaging of the material-specific capacities ($q_{\text{Gr}} = 340 \text{ mAh g}^{-1}$, $q_{\text{Si}} = 3400 \text{ mAh g}^{-1}$) and agree well with the practically achieved capacities.

Materials characterization

Porous electrodes were analyzed by scanning electron microscopy (NVision40, Zeiss). The cross-sectional preparation of the electrodes was performed using the broad ion preparation method (TIC020, Leica). Phase analysis was carried out using a D8 Advance diffractometer (Bruker) with a Cu-K α X-ray tube and a 1D-detector. SEM images of Si electrodes were recorded by use of a scanning electron microscope JSM (JEOL, Japan). To identify crystallinity of columnar silicon anodes, Raman spectroscopy was performed using a Raman microscope (micro-Raman Spectrometer, Renishaw inVia PLC) at an excitation laser wavelength of 514 nm and a 50 \times objective. The laser beam was aligned onto the sample with a density and acquisition time of 0.44 mW/ μ m and 5 \times 60 s, respectively. The powder XRD (Cu-K α , 40 V, 40 mA) diffractogram was acquired for Si anode using a D005 XRD system (Siemens, Germany).

Acknowledgements

This work was supported by the German Federal Ministry of Education and Research (BMBF) in the framework of the project KaSiLi (Grant No. 03XP0254). Open Access funding enabled and organized by Projekt DEAL.

Conflict of Interest

The authors declare no conflict of interest.

Keywords: batteries • blended electrodes • graphite • silicon • energy storage

- [1] S. Goriparti, E. Miele, F. de Angelis, E. Di Fabrizio, R. Proietti Zaccaria, C. Capiglia, *J. Power Sources* **2014**, 257, 421.
- [2] W.-J. Zhang, *J. Power Sources* **2011**, 196, 13.
- [3] N. Nitta, F. Wu, J. T. Lee, G. Yushin, *Mater. Today* **2015**, 18, 252.
- [4] R. Marom, S. F. Amalraj, N. Leifer, D. Jacob, D. Aurbach, *J. Mater. Chem.* **2011**, 21, 9938.
- [5] S. De, P. W. Northrop, V. Ramadesigan, V. R. Subramanian, *J. Power Sources* **2013**, 227, 161.
- [6] J. Ye, A. C. Baumgaertel, Y. M. Wang, J. Biener, M. M. Biener, *ACS Nano* **2015**, 9, 2194.
- [7] C. Heubner, T. Liebmann, M. Schneider, A. Michaelis, *Electrochim. Acta* **2018**, 269, 745.
- [8] S. Luo, K. Wang, J. Wang, K. Jiang, Q. Li, S. Fan, *Adv. Mater.* **2012**, 24, 2294.
- [9] G. Liu, S. Xun, N. Vukmirovic, X. Song, P. Olalde-Velasco, H. Zheng, V. S. Battaglia, L. Wang, W. Yang, *Adv. Mater.* **2011**, 23, 4679.
- [10] M. Roberts, P. Johns, J. Owen, D. Brandell, K. Edstrom, G. El Enany, C. Guery, D. Golodnitsky, M. Lace, C. Lecoeur, H. Mazor, E. Peled, E. Perre, M. M. Shajumon, P. Simon, P.-L. Taberna, *J. Mater. Chem.* **2011**, 21, 9876.
- [11] T. S. Arthur, D. J. Bates, N. Cirigliano, D. C. Johnson, P. Malati, J. M. Mosby, E. Perre, M. T. Rawls, A. L. Prieto, B. Dunn, *MRS Bull.* **2011**, 36, 523.
- [12] C. Heubner, S. Reuber, J. Seeba, P. Marcinkowski, K. Nikolowski, M. Schneider, M. Wolter, A. Michaelis, *J. Power Sources* **2020**, 479, 228704.
- [13] X. Zuo, J. Zhu, P. Müller-Buschbaum, Y.-J. Cheng, *Nano Energy* **2017**, 31, 113.
- [14] X. Su, Q. Wu, J. Li, X. Xiao, A. Lott, W. Lu, B. W. Sheldon, J. Wu, *Adv. Energy Mater.* **2014**, 4, 1300882.
- [15] Z. Zeng, N. Liu, Q. Zeng, S. W. Lee, W. L. Mao, Y. Cui, *Nano Energy* **2016**, 22, 105.
- [16] M. Wetjen, S. Solchenbach, D. Pritzl, J. Hou, V. Tileli, H. A. Gasteiger, *J. Electrochem. Soc.* **2018**, 165, A1503-A1514.
- [17] X. H. Liu, Li Zhong, S. Huang, S. X. Mao, T. Zhu, J. Y. Huang, *ACS Nano* **2012**, 6, 1522.
- [18] M. N. Obrovac, L. Christensen, *Electrochim. Solid-State Lett.* **2004**, 7, A93.
- [19] A. L. Michan, G. Divitini, A. J. Pell, M. Leskes, C. Ducati, C. P. Grey, *J. Am. Chem. Soc.* **2016**, 138, 7918.
- [20] E. Radvanyi, W. Porcher, E. de Vito, A. Montani, S. Franger, S. Jouanneau Si Larbi, *Phys. Chem. Chem. Phys.* **2014**, 16, 171142.
- [21] M. Nie, D. P. Abraham, Y. Chen, A. Bose, B. L. Lucht, *J. Phys. Chem. C* **2013**, 117, 13403.
- [22] C. Xu, F. Lindgren, B. Philippe, M. Gorgoi, F. Björefors, K. Edström, T. Gustafsson, *Chem. Mater.* **2015**, 27, 2591.
- [23] C. C. Nguyen, T. Yoon, D. M. Seo, P. Guduru, B. L. Lucht, *ACS Appl. Mater. Interfaces* **2016**, 8, 12211.
- [24] J. Bareño, I. A. Shkrob, J. A. Gilbert, M. Klett, D. P. Abraham, *J. Phys. Chem. C* **2017**, 121, 20640.
- [25] H. Kim, B. Han, J. Choo, J. Cho, *Angew. Chem.* **2008**, 120, 10305.
- [26] H. Ma, F. Cheng, J.-Y. Chen, J.-Z. Zhao, C.-S. Li, Z.-L. Tao, J. Liang, *Adv. Mater.* **2007**, 19, 4067.
- [27] C. K. Chan, H. Peng, G. Liu, K. McIlwrath, X. F. Zhang, R. A. Huggins, Y. Cui, *Nat. Nanotechnol.* **2008**, 3, 31.
- [28] C. Heubner, U. Langklotz, A. Michaelis, *J. Energy Storage* **2018**, 15, 181.
- [29] S. Cangaz, F. Hippauf, F. S. Reuter, S. Doerfler, T. Abendroth, H. Althues, S. Kaskel, *Adv. Energy Mater.* **2020**, 10, 2001320.
- [30] A. Baasner, F. Reuter, M. Seidel, A. Krause, E. Pflug, P. Härtel, S. Dörfler, T. Abendroth, H. Althues, S. Kaskel, *J. Electrochem. Soc.* **2020**, 167, 20516.
- [31] H. Zhao, Y. Wei, C. Wang, R. Qiao, W. Yang, P. B. Messersmith, G. Liu, *ACS Appl. Mater. Interfaces* **2018**, 10, 5440.
- [32] P.-F. Cao, M. Naguib, Z. Du, E. Stacy, B. Li, T. Hong, K. Xing, D. N. Voylov, J. Li, D. L. Wood, A. P. Sokolov, J. Nanda, T. Saito, *ACS Appl. Mater. Interfaces* **2018**, 10, 3470.
- [33] M. Klett, J. A. Gilbert, K. Z. Pupek, S. E. Trask, D. P. Abraham, *J. Electrochem. Soc.* **2017**, 164, A6095-A6102.
- [34] Y. Zhang, X. G. Zhang, H. L. Zhang, Z. G. Zhao, F. Li, C. Liu, H. M. Cheng, *Electrochim. Acta* **2006**, 51, 4994.
- [35] P. Li, H. Kim, S.-T. Myung, Y.-K. Sun, *Energy Storage Mater.* **2021**, 35, 550.
- [36] Q. Shi, J. Zhou, S. Ullah, X. Yang, K. Tokarska, B. Trzebicka, H. Q. Ta, M. H. Rümmeli, *Energy Storage Mater.* **2021**, 34, 735.
- [37] M. A. Azam, N. E. Safie, A. S. Ahmad, N. A. Yuza, N. S. A. Zulkifli, *J. Energy Storage* **2021**, 33, 102096.
- [38] S. Chae, S.-H. Choi, N. Kim, J. Sung, J. Cho, *Angew. Chem. Int. Ed. Engl.* **2020**, 59, 110.
- [39] S. B. Chikkannanavar, D. M. Bernardi, L. Liu, *J. Power Sources* **2014**, 248, 91.
- [40] C. Heubner, T. Liebmann, C. Lämmel, M. Schneider, A. Michaelis, *J. Energy Storage* **2018**, 20, 101.
- [41] C. L. Berhaut, D. Z. Dominguez, P. Kumar, P.-H. Jouneau, W. Porcher, D. Aradilla, S. Tardif, S. Pouget, S. Lyonnard, *ACS Nano* **2019**, 13, 11538.
- [42] K. P. C. Yao, J. S. Okasinski, K. Kalaga, J. D. Almer, D. P. Abraham, *Adv. Energy Mater.* **2019**, 9, 1803380.
- [43] P.-F. Lory, B. Mathieu, S. Genies, Y. Reynier, A. Boulineau, W. Hong, M. Chandresris, *J. Electrochem. Soc.* **2020**, 167, 120506.
- [44] K. Richter, T. Waldmann, N. Paul, N. Jobst, R.-G. Scurtu, M. Hofmann, R. Gilles, M. Wohlfahrt-Mehrens, *ChemSusChem* **2020**, 13, 529.
- [45] J. Moon, H. C. Lee, H. Jung, S. Wakita, S. Cho, J. Yoon, J. Lee, A. Ueda, B. Choi, S. Lee, K. Ito, Y. Kubo, A. C. Lim, J. G. Seo, J. Yoo, S. Lee, Y. Ham, W. Baek, Y.-G. Ryu, I. T. Han, *Nat. Commun.* **2021**, 12, 2714.
- [46] C. Heubner, T. Liebmann, C. Lämmel, M. Schneider, A. Michaelis, *ChemElectroChem* **2018**, 5, 425.
- [47] T. Liebmann, C. Heubner, C. Lämmel, M. Schneider, A. Michaelis, *ChemElectroChem* **2019**, 6, 5728.
- [48] S. Ko, J.-I. Lee, H. S. Yang, S. Park, U. Jeong, *Adv. Mater.* **2012**, 24, 4451.
- [49] W. Yuan, Z. Qiu, Y. Chen, B. Zhao, M. Liu, Y. Tang, *Electrochim. Acta* **2018**, 267, 150.
- [50] Y. Xu, Y. Zhu, Y. Liu, C. Wang, *Adv. Energy Mater.* **2013**, 3, 128.
- [51] T. Palaniselvam, M. Goktas, B. Anothumakkool, Y.-N. Sun, R. Schmuck, Li Zhao, B.-H. Han, M. Winter, P. Adelhelm, *Adv. Funct. Mater.* **2019**, 29, 1900790.
- [52] C. Ma, J. Xu, J. Alvarado, B. Qu, J. Somerville, J. Y. Lee, Y. S. Meng, *Chem. Mater.* **2015**, 27, 5633.
- [53] Y. Zhang, P. Zhu, L. Huang, J. Xie, S. Zhang, G. Cao, X. Zhao, *Adv. Funct. Mater.* **2015**, 25, 481.

- [54] C. Heubner, T. Liebmann, C. Lämmel, M. Schneider, A. Michaelis, *J. Power Sources* **2017**, *363C*, 311.
- [55] F. Reuter, A. Baasner, J. Pampel, M. Piwko, S. Dörfler, H. Althues, S. Kaskel, *J. Electrochem. Soc.* **2019**, *166*, A3265-A3271.
- [56] F. Hippauf, B. Schumm, S. Doerfler, H. Althues, S. Fujiki, T. Shiratsuchi, T. Tsujimura, Y. Aihara, S. Kaskel, *Energy Storage Mater.* **2019**, *21*, 390.
- [57] M. Piwko, S. Thieme, C. Weller, H. Althues, S. Kaskel, *J. Power Sources* **2017**, *362*, 349.
- [58] M. Piwko, T. Kuntze, S. Winkler, S. Straach, P. Härtel, H. Althues, S. Kaskel, *J. Power Sources* **2017**, *351*, 183.
- [59] I. Yoon, D. P. Abraham, B. L. Lucht, A. F. Bower, P. R. Guduru, *Adv. Energy Mater.* **2016**, *6*, 1600099.
- [60] B. Jerliu, E. Hüger, L. Dörner, B. K. Seidlhofer, R. Steitz, M. Horisberger, H. Schmidt, *Phys. Chem. Chem. Phys.* **2018**, *20*, 23480.
- [61] A. Reyes Jiménez, R. Klöpsch, R. Wagner, U. C. Rodehorst, M. Kolek, R. Nölle, M. Winter, T. Placke, *ACS Nano* **2017**, *11*, 4731.
- [62] T. Yoon, C. C. Nguyen, D. M. Seo, B. L. Lucht, *J. Electrochem. Soc.* **2015**, *162*, A2325-A2330.
- [63] S. Misra, N. Liu, J. Nelson, S. S. Hong, Y. Cui, M. F. Toney, *ACS Nano* **2012**, *6*, 5465.
- [64] T. D. Hatchard, J. R. Dahn, *J. Electrochem. Soc.* **2004**, *151*, A838.
- [65] T. Kim, S. Park, S. M. Oh, *J. Electrochem. Soc.* **2007**, *154*, A1112.
- [66] V. P. Phan, B. Pecquenard, F. Le Cras, *Adv. Funct. Mater.* **2012**, *22*, 2580.
- [67] Q. Pan, P. Zuo, T. Mu, C. Du, X. Cheng, Y. Ma, Y. Gao, G. Yin, *J. Power Sources* **2017**, *347*, 170.
- [68] S. P. Nadimpalli, V. A. Sethuraman, S. Dalavi, B. Lucht, M. J. Chon, V. B. Shenoy, P. R. Guduru, *J. Power Sources* **2012**, *215*, 145.
- [69] R. Fong, U. Sacken, Dahn J. R., *J. Electrochem. Soc.*, **1990**, 2009.
- [70] K. Persson, Y. Hinuma, Y. S. Meng, A. van der Ven, G. Ceder, *Phys. Rev. B* **2010**, *82*.
- [71] Gerbrand Ceder, Anton Van der Ven, *Electrochim. Acta* **1999**, *45*, 131.
- [72] D. Allart, M. Montaru, H. Gualous, *J. Electrochem. Soc.* **2018**, *165*, A380-A387.
- [73] J. R. Dahn, *Phys. Rev. B* **1991**, *44*, 9170.
- [74] C. Heubner, C. Lämmel, A. Nickol, T. Liebmann, M. Schneider, A. Michaelis, *J. Power Sources* **2018**, *397*, 11.
- [75] R. Tian, P. J. King, J. Coelho, S.-H. Park, D. V. Horvath, V. Nicolosi, C. O'Dwyer, J. N. Coleman, *J. Power Sources* **2020**, *468*, 228220.
- [76] C. Heubner, K. Nikolowski, S. Reuber, M. Schneider, M. Wolter, A. Michaelis, *Batteries & Supercaps* **2020**, *4*, 268.
- [77] C. Heubner, M. Schneider, A. Michaelis, *Adv. Energy Mater.* **2020**, *10*, 1902523.
- [78] F. Jeschull, Y. Surace, S. Zürcher, G. Lari, M. E. Spahr, P. Novák, S. Trabesinger, *J. Electrochem. Soc.* **2020**, *167*, 100535.
- [79] J. Wu, Y. Cao, H. Zhao, J. Mao, Z. Guo, *Carbon Energy* **2019**, *1*, 57.
- [80] Y. Zhang, X. G. Zhang, H. L. Zhang, Z. G. Zhao, F. Li, C. Liu, H. M. Cheng, *Electrochim. Acta* **2006**, *51*, 4994.

Manuscript received: July 26, 2021

Revised manuscript received: September 30, 2021

Accepted manuscript online: October 1, 2021

Version of record online: October 20, 2021